Cell Reports
Physical Science

CellPress
OPEN ACCESS

Article

# Self-assembled conformal $SnO_2$ electron transport layer via targeted chelating enables efficient, scalable, and stable perovskite solar cells

Hongzhen Su,[1,2] Xuesong Lin,[3,4] Li He,[1,2] Chao Gao,[1,2] Dezhao Zhang,[1,2] Haotian Zhang,[1,2] Daxue Du,[1,2] Hong Liu,[1,2] and Wenzhong Shen[1,2,5,6,*]

[1]Institute of Solar Energy and Key Laboratory of Artificial Structures and Quantum Control (Ministry of Education), School of Physics and Astronomy, Shanghai Jiao Tong University, Shanghai 200240, P.R. China
[2]Shanghai Non-carbon Energy Conversion and Utilization Institute, Shanghai 200240, P.R. China
[3]School of Materials Science and Engineering, Shanghai Jiao Tong University, Shanghai 200240, P.R. China
[4]Contemporary Amperex Technology Co. Limited (CATL), Ningde 352000, P.R. China
[5]Collaborative Innovation Center of Advanced Microstructures, Nanjing 210093, P.R. China
[6]Lead contact
*Correspondence: wzshen@sjtu.edu.cn
https://doi.org/10.1016/j.xcrp.2025.102506

## SUMMARY

Balance between coverage and performance in the electron transport layer (ETL) is crucial for maximizing the efficiency, scalability, and stability of large-area perovskite solar cells (PSCs). Here, a solution-based targeted chelating strategy is designed to construct a self-assembled conformal $SnO_2$ ETL on a textured transparent conductive oxide surface with submicron roughness. By fine-tuning the molecular architecture, the targeted chelating molecule with two-electron-donating group and conjugated structure, capable of electron redistribution, can bridge the targeted $V_O$ of $SnO_2$ nanoparticles and $F_O$ of transparent conductive oxide, respectively, which balances the interface charge dynamics. The use of a self-assembled conformal $SnO_2$ ETL modified with targeted chelating molecules enabled PSCs with efficiencies of 25.32% and 24.57% on aperture areas of 0.09 and 1.00 $cm^2$, respectively, and 1,600-h operational stability based on the ISOS-L-3 protocol (maximum power point, continuous 1 sun illumination, 65°C, and ca. 50% relative humidity).

## INTRODUCTION

Perovskite solar cells (PSCs) have attracted widespread attention due to their rapid increase in power-conversion efficiency (PCE).[1–4] This is mainly attributed to the development and optimization of electron transport layers (ETLs), particularly $SnO_2$ ETLs.[3,5–7] However, the state-of-the-art PCEs are mostly achieved in devices with small aperture areas (<0.1 $cm^2$).[8] To realize the commercialization of PSCs, efforts to enhance the uniformity of perovskite,[9–11] passivation layers,[12] and hole transport layers (HTLs)[13,14] have been made to improve the PCE of large-area devices. However, the major challenge hindering the commercial viability of PSCs lies in achieving large-scale and uniform deposition of the ETL.

Various methods such as slot-die coating,[15] blade coating,[16] spray coating,[17] chemical bath deposition (CBD),[18] and atomic layer deposition[19] have been proposed to prepare uniform $SnO_2$ ETLs. Among these, CBD stands out as a cost-effective and low-temperature fabrication method. Researchers have demonstrated ideal coverage, thickness, and composition of $SnO_2$ layers by controlling the decomposition pathway of $SnCl_2$ during the CBD process and have achieved a champion PCE of over 25% (aperture area, 0.09 $cm^2$).[3] However, the CBD method is accompanied by strict control required during the process, and the PCE of devices prepared using the CBD method still decreases rapidly with increasing device area.[20,21]

Compared to the precise control required for CBD, the solution-based method for preparing an ETL is more easily controllable on a large scale and is compatible with existing industrial processes such as blade coating and slot-die coating. However, it is very challenging to fabricate a large-area and thin ETL with a conformal coverage of $SnO_2$ nanoparticles on textured transparent conductive oxide (TCO) substrates.[22–25] This is primarily due to the need for substrates with improved lateral transport properties but larger roughness for large-area devices,[26] although researchers utilized the interaction between the polymer polyacrylic acid and metal oxides to achieve conformal coverage of $SnO_2$ nanoparticles on a compact $TiO_2$ layer, and a corresponding small-area device (aperture area, 0.08 $cm^2$) achieved a PCE of 25.7% with a high fill factor (FF) of 83.84%.[27] The FF and PCE decreased to 79.05% and 23.25%, respectively, when the aperture area increased to 1 $cm^2$. This decrease in performance is mainly attributed to the high-resistance polymer, which is unable to accurately selectively connect $SnO_2$ and the metal oxides on the substrate, respectively, resulting in a large amount of polymer that only binds with $SnO_2$ and

Please cite this article in press as: Su et al., Self-assembled conformal $SnO_2$ electron transport layer via targeted chelating enables efficient, scalable, and stable perovskite solar cells, Cell Reports Physical Science (2025), https://doi.org/10.1016/j.xcrp.2025.102506



remains inside the ETL layer. This residual polymer is challenging to remove during the annealing process and may introduce additional defects and adversely affect the conductivity of the $SnO_2$ layer, thereby increasing the series resistance of the device.[28,29] Therefore, an accurate strategy to achieve targeted chelation between ETL and substrate and realize a self-assembled conformal ETL is necessary for addressing the trade-off between coverage and performance in ETLs for large-area devices.

Here, we propose a targeted chelating strategy to realize a self-assembled conformal $SnO_2$ ETL. By fine-tuning the molecular architecture, the targeted chelating molecules (TCMs) featuring a two-electron-donating group and conjugated structure, capable of electron redistribution, can bridge the targeted oxygen vacancies ($V_O$) of $SnO_2$ nanoparticles and F atoms substituting O atoms ($F_O$) of TCO, respectively, thus facilitating the conformal deposition of $SnO_2$ on the textured TCO surface and passivating the surface defect of $SnO_2$. Additionally, the terminal groups of TCMs are coordinated with unsaturated $Pb^{2+}$ ions during the perovskite crystallization, which enhances perovskite crystallinity and interface contact between the ETL and perovskite. Consequently, the TCMs achieve an effective electron transmission path in perovskite/ETL/TCO without introducing additional series resistance by targeted chelating. The resulting devices achieved the champion PCE of 25.32% under reverse scan with an aperture area of 0.09 $cm^2$. With the aperture area expanded to 1.00 $cm^2$, a champion PCE of 24.57% was obtained. Moreover, the encapsulated devices maintained 90% of their initial efficiency after enduring 1,600 h of testing following the ISOS-L-3 protocol (for test details, see methods).

## RESULTS AND DISCUSSION

### First-principles simulations of the targeted chelating strategy

Figure 1A illustrates the self-assembly process of conformal $SnO_2$ using a targeted chelating strategy. The goal is for one terminal group of the TCMs to selectively adsorb onto the surface of $SnO_2$ nanoparticles in the dispersed solution, while another terminal group anchors onto the TCO substrate during the solution preparation of the ETL, resulting in a self-assembled conformal $SnO_2$ ETL with excellent roughness tolerance. Previous research has revealed that the electron-cloud distribution of the molecules plays a crucial role in chelating strength and morphology. Using electron-donating groups, it is possible to bind to positively charged defect sites.[30] Moreover, through control of the conjugated structure within the molecule, the resonance-induced redistribution effect of the electron cloud can be enhanced, which would facilitate targeted chelating at different defect sites.[31–33] We systematically investigated the impact of different electron-donating terminal groups (such as the formate group and phosphate group) and conjugated chain lengths by selecting 4,4′-biphenyldiphosphonic acid (MBBM), 4,4′-biphenylenebisphosphonic acid (PBBP), and 1,4-phenyldiphosphonic acid (PBP) as three TCMs to achieve an optimum conformal $SnO_2$ ETL without introducing unexpected series resistance and shunt paths, which would increase the charge non-radiative recombination at the interfaces or within the ETL. Fluorine-doped tin oxide (FTO), with high surface roughness, has been employed as a representative TCO for further investigation.

The first-principles calculations were utilized to analyze the chelating strength and morphology of different TCMs. Figure 1B shows the different doping mechanisms of $SnO_2$ and FTO. $SnO_2$ is mainly based on self-doping through oxygen vacancies ($V_O$, carrying two positive charges) to achieve an n-type semiconductor, while FTO is mainly based on artificially introduced F atoms substituting O atoms ($F_O$, carrying a single positive charge) to achieve electron conductivity.[34,35] Therefore, the positively charged $V_O$ and $F_O$ will respectively become important chelating points for TCMs with $SnO_2$ and FTO. In Figure 1C, we calculated the adsorption energies of the three TCMs with the $V_O$ defect sites on $SnO_2$ (denoted as $SnO_2$-TCMs) to evaluate the chelation of TCMs and nanoparticles in the $SnO_2$ dispersion. In detail, MBBM, PBBP, and PBP show adsorption energies of −3.44, −6.52, and −6.09 eV, respectively, indicating that all three TCMs tend to bind with $V_O$, and the chelating ability of the phosphate group is stronger than that of the formate group due to its higher electron-cloud density. Moreover, the chelation of PBBP to $V_O$ is stronger than that of PBP, mainly due to the higher electron-cloud redistribution ability of the linked benzene conjugation, resulting in the phosphate group bound to $V_O$ having a higher electron-cloud density (Figure S1). The optimized $SnO_2$-TCM structures (Figures 1D and S2) further demonstrate that MBBM and $V_O$ exhibit a double-bonded chelating structure, while PBBP and PBP exhibit a triple-bonded chelating structure, which indicates stronger chelating strength induced by the phosphate group and electron-cloud redistribution.

It is worth noting that there is still a remaining terminal group in the $SnO_2$-TCM structure, and its capability of strong chelation to the surface of $SnO_2$ nanoparticles in the dispersion could lead to the aggregation of nanoparticles and forbid the next chelation to FTO. Therefore, we optimized model structures of different $SnO_2$-TCMs chelating to another $V_O$ defect site (Figure S3) and calculated the adsorption energies of the above chelating process (Figure 1E). The terminal-group adsorption energies of $SnO_2$-MBBM and $SnO_2$-PBP showed a slight decrease by 0.04 and 0.11 eV, respectively, indicating that the terminal groups of these two structures still possess considerable chelating capability. In contrast, the terminal-group adsorption energy of $SnO_2$-PBBP decreased by 6.2 eV. Compared to the phosphate group in PBBP, the chelating capability of the remaining group in $SnO_2$-PBBP significantly decreased, which resulted from the stronger electron-cloud redistribution ability of the phenyl-conjugated structure. This phenomenon led to a weakened electron-donating ability of the remaining phosphate group. Compared to MBBM and PBP, PBBP with the above characteristic is expected to form a highly dispersed $SnO_2$ dispersion and provide a reserved terminal group for subsequent chelation to FTO. Notably, there is a competitive relationship between TCMs and $SnO_2$-TCMs chelating to $V_O$, and the possibility for the occurrence of the two reactions can be evaluated based on the Arrhenius equation (details of which are given in Note S2).[36,37] As shown in Figure S4, the above possibilities in the MBBM (51.0%:49.0%) and PBP (52.2%:47.8%) systems are similar, indicating that the above two TCMs are intended to bridge to two $SnO_2$ nanoparticles in the dispersion. In contrast, the

Please cite this article in press as: Su et al., Self-assembled conformal $SnO_2$ electron transport layer via targeted chelating enables efficient, scalable, and stable perovskite solar cells, Cell Reports Physical Science (2025), https://doi.org/10.1016/j.xcrp.2025.102506





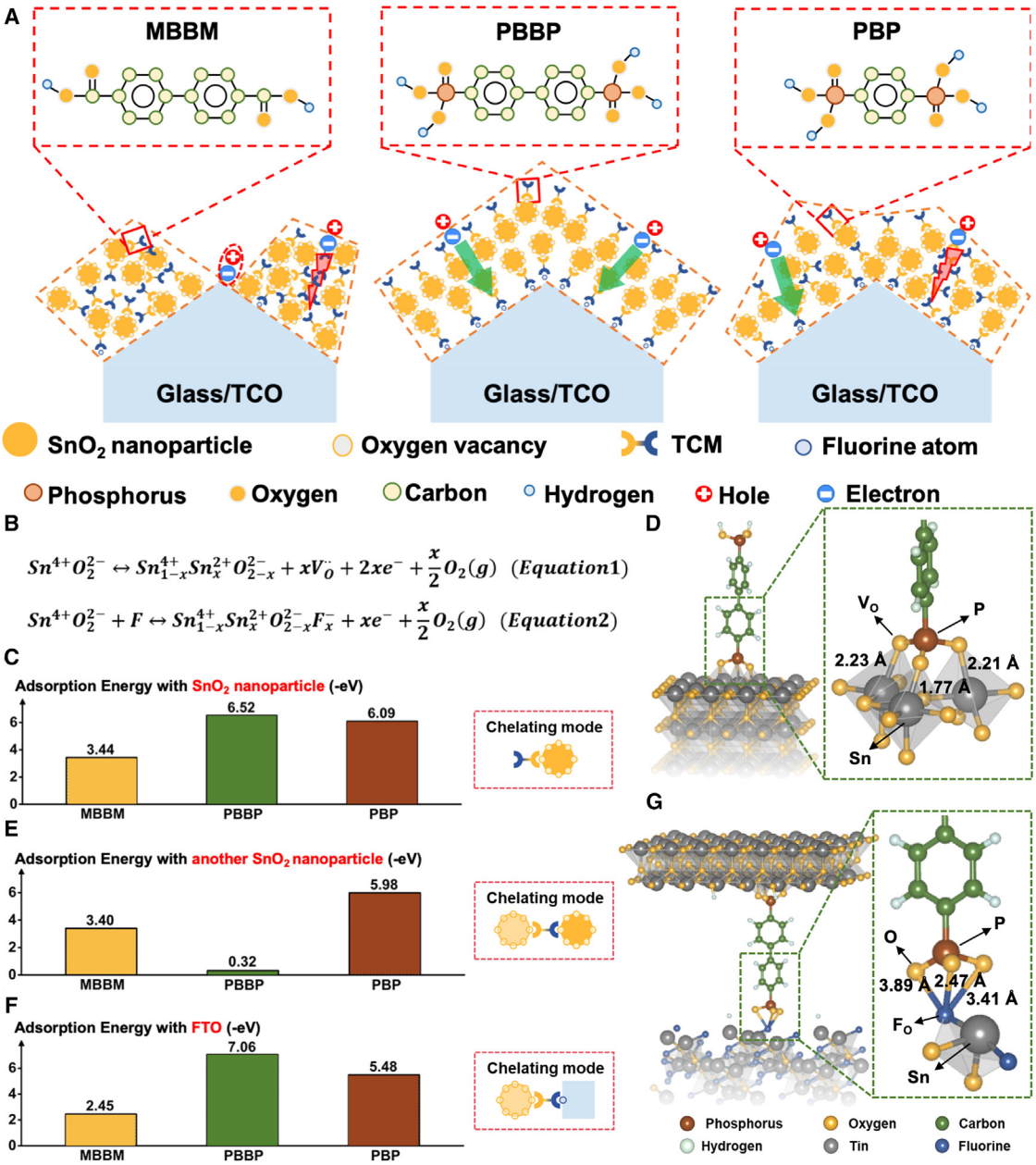


**Figure 1. TCMs induce the formation of self-assembled conformal $SnO_2$ indicated by first-principles simulations**

(A) Schematic depiction of the TCM-induced self-assembled conformal $SnO_2$ on a TCO-glass substrate and the molecular structure of the TCMs with different electron-donating groups and conjugated chains. The red ellipse and red paths represent the charge non-radiative recombination.

(B) Mechanisms for self-doping of $SnO_2$ by $V_O$ and ex-doping of FTO by $F_O$.

(C) Simulated adsorption energy of TCMs with $SnO_2$ nanoparticle.

(D) Optimized chelating structure between the phosphate group of PBBP and $V_O$ of $SnO_2$ nanoparticles.

(E and F) Simulated adsorption energy of $SnO_2$-TCMs with (E) $SnO_2$ nanoparticles and (F) FTO.

(G) Optimized chelating structure between the phosphate group of $SnO_2$-PBBP and $F_O$ of FTO substrate. Inset marks the critical elements and corresponding bond lengths.

possibility of chelating one particle (99.8%) is nearly 500 times higher than that of chelating to two particles (0.2%) in the PBBP system, indicating the tendency for the formation of $SnO_2$-PBBP structure and reduction of nanoparticle aggregation in $SnO_2$ dispersion.

As the step of $SnO_2$-dispersion deposition on the FTO substrate to form the ETL, the structures and adsorption energies of $SnO_2$-TCMs chelated to the $F_O$ defect sites on the FTO surface were considered. As shown in Figure 1F, $SnO_2$-PBBP exhibits the strongest chelating ability to the $F_O$ defect site (adsorption

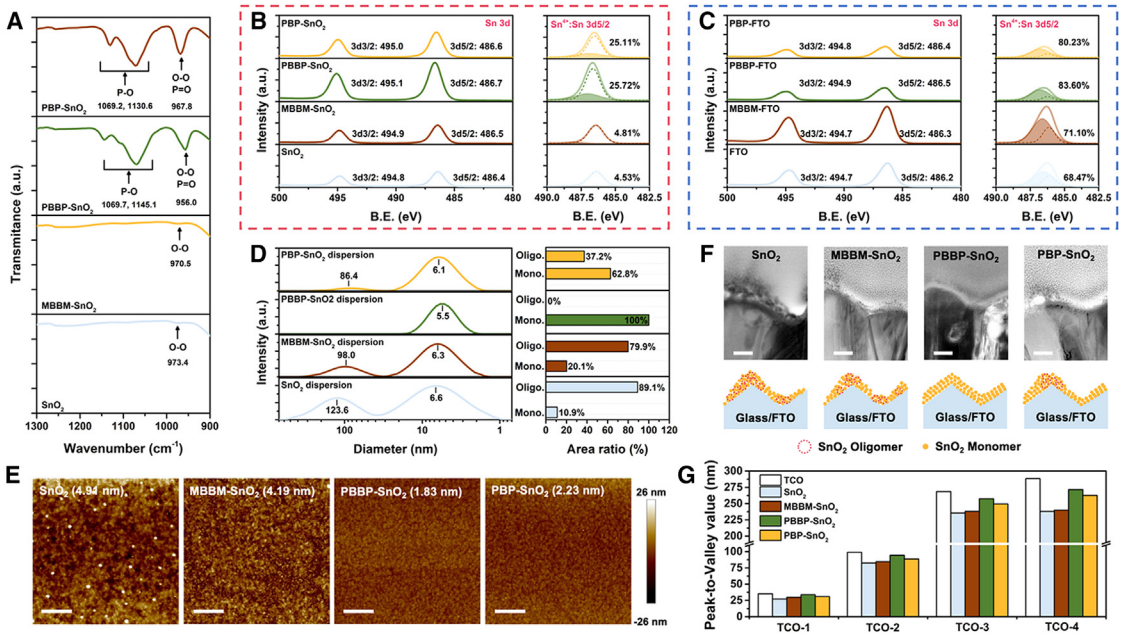


**Figure 2. TCMs induce the quasi-monomer distribution and conformal coverage of $SnO_2$**

(A) ATR-IR spectra of $SnO_2$ ETL modified with or without TCMs atop $BaF_2$ substrates.

(B and C) XPS of Sn 3d core level of (B) $SnO_2$ ETL modified with or without TCMs atop glass and (C) FTO covered with or without TCMs. Right-hand panels are zoomed-in Sn $3d_{5/2}$ peaks. Shaded area, dashed line, and solid line represent the $Sn^{4+}$ peak, $Sn^{2+}$ peak, and total peak of the Sn $3d_{5/2}$ core level, respectively. The inset value shows the proportion of the peak area occupied by the $Sn^{4+}$ peak.

(D) DLS spectra of $SnO_2$ dispersion modified with or without TCMs. Right-hand panel summarizes the area ratio of oligomer and monomer, abbreviated as Oligo. and Mono., respectively.

(E) AFM images of $SnO_2$ ETL modified with or without TCMs atop Si wafer. Scale bars, 1 μm.

(F) Cross-sectional TEM images of $SnO_2$ ETL with or without TCMs atop FTO. The scale bars represent 50 nm, and the bottom panels schematically illustrate different $SnO_2$ nanoparticles with varying conformality on FTO.

(G) Effects of TCM-$SnO_2$ on peak-to-valley value of different TCO substrates. Note that TCO-3 is the FTO substrate used in this work.

energy −7.06 eV), mainly attributed to the reduced repulsion between F atoms and the reserved phosphate group of PBBP, which exhibits a lower electron-cloud density compared to that of the PBP counterpart.[38] Moreover, the average bond length of the $SnO_2$-PBBP-FTO structure (3.26 Å) is shorter than that of $SnO_2$-PBP-FTO structures (3.35 Å), which originates from the electron-cloud redistribution, as shown in Figures 1G, S1, and S5. As shown in Figure S6, the possibilities of occurrence of three types of $SnO_2$-TCM chelated with $SnO_2$ and FTO were further compared, which indicated that the chelating process of $SnO_2$-PBBP shows the highest selectivity (0.1%:99.9%). PBBP that tends to target chelate to $SnO_2$ and FTO without aggregating inside the $SnO_2$ layer is intended to form a self-assembled $SnO_2$ ETL with enhanced conformality, which would prevent the shunt paths, reduce the series resistance, and modify the interface charge dynamics.[39]

## Distribution and conformality of $SnO_2$

Before analyzing the effect of TCMs on distribution of $SnO_2$ dispersion and the conformation of the corresponding ETL, the pH values of the TCM aqueous solutions were adjusted to be consistent with the alkaline dispersing $SnO_2$. After the modification, the uniform, clear, and stable TCM-$SnO_2$ dispersions are formed, referred to as MBBM-$SnO_2$, PBBP-$SnO_2$, and PBP-$SnO_2$ dispersions, respectively (Figure S7 and Table S1; for details see Notes S4 and S5).

The interaction between TCMs and $SnO_2$ was characterized by using attenuated total reflectance infrared (ATR-IR) spectroscopy. As shown in Figure 2A, compared to the $SnO_2$ sample, the O–O vibration peaks of MBBM-$SnO_2$, PBBP-$SnO_2$ and PBP-$SnO_2$ all shifted toward lower wavenumbers by 2.9, 17.4, and 5.6 $cm^{-1}$, respectively. Additionally, both PBBP-$SnO_2$ and PBP-$SnO_2$ showed significant P–O vibration peaks. Both results indicate the strongest interaction between PBBP and $SnO_2$, followed by PBP and MBBM. Furthermore, we further analyzed the uniformity of O–O and P–O vibrations using Fourier transform infrared (FTIR) mapping, as shown in Figure S8. It is evident that the evolution of uniformity of vibration peaks is consistent with the strength of interactions obtained in Figure 2A, where PBBP-$SnO_2$ shows the highest uniformity in the distribution of O–O and P–O vibration peaks. Compared to $SnO_2$, the uniformity of MBBM-$SnO_2$ and PBP-$SnO_2$ has been improved, but there still remains obvious aggregation. As shown in Figure 1C, the doping mechanism of $SnO_2$ and FTO will result in a decrease in the apparent oxidation state of Sn element and introduce defect states related to O ($V_O$ and $F_O$), thereby causing a decrease in the apparent reduction state of O element. Therefore, X-ray photoelectron spectroscopy (XPS) characterization

Please cite this article in press as: Su et al., Self-assembled conformal $SnO_2$ electron transport layer via targeted chelating enables efficient, scalable, and stable perovskite solar cells, Cell Reports Physical Science (2025), https://doi.org/10.1016/j.xcrp.2025.102506



of the Sn 3d and O 1s characteristic peaks was carried out to confirm that the chelating sites of TCMs on $SnO_2$ and FTO are $V_O$ and $F_O$, respectively. As shown in the left panel of Figure 2B, the interaction of TCMs with $SnO_2$ causes the Sn 3d peak to shift toward higher binding energies, with PBBP-$SnO_2$ showing the largest shift (0.3 eV), which indicates that the interaction of PBBP with $SnO_2$ can significantly enhance the oxidation state of Sn. Further analysis of the Sn $3d_{5/2}$ peak revealed that it can be decoupled into $Sn^{4+}$ (486.6 eV) and $Sn^{2+}$ (486.1 eV) peaks (right panel, Figure 2B). The proportion of $Sn^{4+}$ of PBBP-$SnO_2$ was increased to 25.72%, compared with 4.53% of $SnO_2$ sample. Similarly, as shown in Figure 2C, the interactions of TCMs with FTO also enhanced the oxidation state of Sn element. Compared to $SnO_2$ with $Sn^{4+}$ proportion of 68.47%, PBBP-FTO exhibited the highest $Sn^{4+}$ proportion of 83.60%, followed by PBP (80.23%) and MBBM (71.10%). As shown in Figure S9, the O 1s peak can be decoupled into defect oxygen ($O_{defect}$, 529.9 eV) and lattice oxygen ($O_{lattice}$, 531.1 eV) peaks. TCMs can reduce the proportion of $O_{defect}$ of $SnO_2$ ($V_O$) and FTO ($F_O$), and the evolution trend was contrary to that observed for $Sn^{4+}$ proportion of the Sn 3d peak (Figures 2B and 2C). These results indicate that the chelating sites of TCMs on $SnO_2$ and FTO are $V_O$ and $F_O$, respectively, with PBBP demonstrating the champion chelating performance.

Dynamic light scattering (DLS) was applied to characterize the impact of different TCMs on the distribution mode of $SnO_2$ nanoparticles in $SnO_2$ dispersion. As shown in Figure 2D, the $SnO_2$ dispersion exhibited severe aggregation, with $SnO_2$ oligomers (peak diameter at 123.6 nm) accounting for 89.1%, while $SnO_2$ monomers merely accounted for 10.9%. After adjustment with MBBM and PBP in the $SnO_2$ dispersion, the peak diameter of oligomers gradually decreased to 98.0 and 86.4 nm, with proportions also decreasing to 79.9% and 37.2%, respectively, while two diameter peaks were still observed. In contrast, the PBBP-$SnO_2$ dispersion showed only a peak for $SnO_2$ monomers with a peak diameter of 5.5 nm, indicating the formation of a quasi-monomer distribution. The schematic distribution of nanoparticles in the four types of $SnO_2$ dispersions is shown in Figure S10. Further statistical analysis of the nanoparticle size using transmission electron microscopy (TEM) revealed that the average grain size (AGS) of $SnO_2$ nanoparticles in all dispersions was approximately 4 nm, similar to the peak diameter of $SnO_2$ monomer (Figure S11). These results indicate that PBBP only reduces the $SnO_2$ aggregation without altering the size of $SnO_2$ nanoparticles, which induces the formation of quasi-monomer distribution. To observe the impact of $SnO_2$ aggregation on the roughness of an ETL, the four types of dispersions were spin coated on smooth silicon wafer (roughness less than 1 nm). As shown in Figure 2E, PBBP-$SnO_2$ film shows the lowest surface roughness of 1.83 nm compared to $SnO_2$ (4.91 nm), MBBM-$SnO_2$ (4.19 nm), and PBP-$SnO_2$ (2.23 nm) measured by atomic force microscopy (AFM), thus demonstrating the excellent film-forming properties of the quasi-monomer PBBP-$SnO_2$ dispersion.

As shown in Figure 2F, the cross-sectional TEM morphologies of the four types of ETLs on FTO exhibit drastically different conformality, as illustrated in the schematic at the bottom of the figure. The thickness of the $SnO_2$ ETL on FTO varies obviously between peaks and valleys, which displays a severe aggregation phenomenon. Compared with the $SnO_2$ ETL, the conformality of MBBM-$SnO_2$ and PBP-$SnO_2$ have been improved, primarily due to reduced aggregation in the dispersions. In comparison, the dispersion of PBBP-$SnO_2$ on FTO facilitates the construction of a highly conformal and uniform ETL, mainly attributed to quasi-monomer dispersion induced by PBBP and its excellent chelating ability to FTO. The corresponding energy-dispersive spectra (EDS) are shown in Figure S12. These results are consistent with the results of first-principles calculations (Figure 1). The top-view scanning electron microscopy (SEM) images with expanded scale also demonstrate the conformal morphology of PBBP-$SnO_2$ on FTO substrates (Figure S13). Compared to the $SnO_2$ ETLs, TCM-$SnO_2$ ETLs atop FTO show a slight improvement in transmittance and conductivity, primarily attributed to reduced light scattering resulting from improved conformality and reduced electron scattering by defect chelating (Figure S14). To further demonstrate the conformality of PBBP-$SnO_2$ ETLs, four types of TCO substrate with different peak-to-valley values were selected and named TCO-1 (35 nm), TCO-2 (100 nm), TCO-3 (FTO, 270 nm), and TCO-4 (290 nm). As shown in Figure 2G, compared to the $SnO_2$ ETL, both MBBM-$SnO_2$ and PBP-$SnO_2$ ETLs show improved conformality on four types of TCO. However, as the peak-to-valley values of TCO increase, the conformality of these ETLs significantly deteriorates. In contrast, PBBP-$SnO_2$ ETLs consistently exhibit the most outstanding conformal capabilities even as the peak-to-valley values of TCO substrates vary between 35 nm (TCO-1) and 290 nm (TCO-4). This property is intended to eliminate interface shunt paths and non-radiative recombination between TCO and perovskite.

## Balance of the interface carrier dynamics

In addition to conformality, the charge transport performance and the effect of ETLs on perovskite will greatly affect the interface carrier dynamics. The interface energy mismatching of conduction band minimum (CBM) (>0.2 eV) between the ETL and perovskite will lead to an open-circuit voltage ($V_{OC}$) loss.[40] On the other hand, an excessive energy mismatch (>0.4 eV) between the CBMs of the ETL and work function (WF) of FTO will result in a Schottky barrier, thereby deteriorating carrier-collection efficiency.[41,42] The characterization of the energy band structure of perovskite, ETLs, and FTO was performed by ultraviolet photoelectron spectroscopy (UPS) and photoluminescence (PL) spectroscopy, including CBMs, WF, and valence band maximum (VBM), as shown in Figures S15 and S16. The detailed values are listed in Table S2. A slight widening of the band gap (0.02–0.2 eV) was observed, which was mainly due to a decrease in the defect state density at the band edges caused by TCM chelation.[43,44] Figure 3A illustrates the energy-level alignment of each layer with the energy mismatch at the perovskite/ETL and ETL/FTO interfaces. With the increase in chelating strength, compared to the $SnO_2$ ETL, the CBM of MBBM-$SnO_2$, PBBP-$SnO_2$, and PBP-$SnO_2$ ETLs all shifted upward by 0.05, 0.22, and 0.09 eV, respectively. These upshifts lead to a reduction in $V_{OC}$ loss caused by interface energy mismatching from 0.36 eV to 0.31, 0.14, and 0.27 eV, respectively, which is confirmed by the xy-plane potential mapping results (Figure S17). Further

Please cite this article in press as: Su et al., Self-assembled conformal $SnO_2$ electron transport layer via targeted chelating enables efficient, scalable, and stable perovskite solar cells, Cell Reports Physical Science (2025), https://doi.org/10.1016/j.xcrp.2025.102506



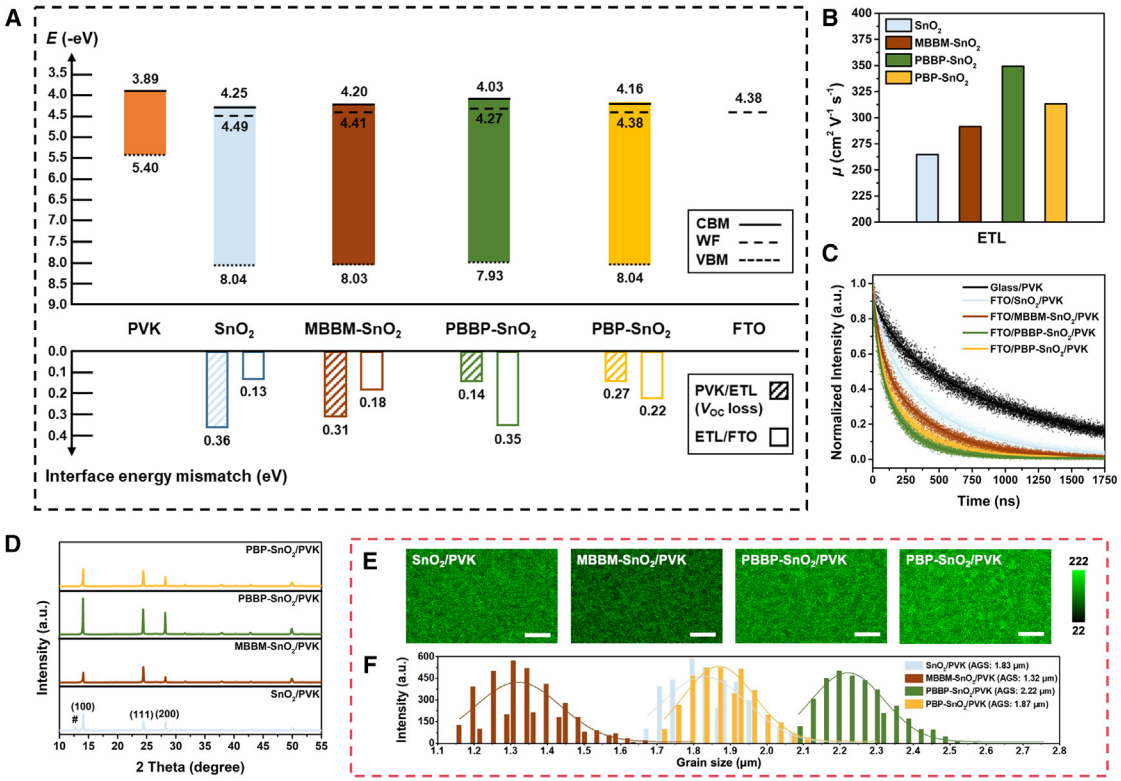


**Figure 3. TCM-$SnO_2$ ETLs balance the interface carrier dynamics**

(A) Energy-level alignment of the perovskite (PVK), $SnO_2$ ETL modified with or without TCMs, and FTO. The bottom panel illustrates the interface energy mismatch between different $SnO_2$ ETLs and perovskite ($V_{OC}$ loss) or FTO.

(B) $\mu$ values of $SnO_2$ ETL modified with or without TCMs. The raw data are shown in Figure S18.

(C) TRPL curves of perovskite atop different substrates.

(D) XRD patterns of perovskite atop different $SnO_2$ ETLs. The characteristic peak of $PbI_2$ is indicated by a hash mark (#).

(E and F) (E) CLSM images and (F) corresponding statistical grain size distribution of perovskite atop different $SnO_2$ ETLs. Scale bars, 10 μm. The AGSs of perovskite atop $SnO_2$, MBBM-$SnO_2$, PBBP-$SnO_2$, and PBP-$SnO_2$ are 1.83, 1.32, 2.22, and 1.87 μm, respectively.

analysis of the energy mismatch at the ETL/FTO interface revealed that the level mismatch of the four ETLs at this interface is less than 0.4 eV, allowing for effective ohmic contact and charge collection. The electron mobility ($\mu$) of the four ETLs was characterized using the space-charge-limited current (SCLC) method, as shown in Note S6 and Figure S18 and summarized in Figure 3B. Compared to the $SnO_2$ ETL (264.7 $cm^2\ V^{-1}\ s^{-1}$), the $\mu$ of MBBM-$SnO_2$, PBBP-$SnO_2$, and PBP-$SnO_2$ ETLs increased to 291.6, 349.2, and 313.3 $cm^2\ V^{-1}\ s^{-1}$, respectively. The improvement was mainly attributed to the passivation of TCMs on surface defects of $SnO_2$ nanoparticles, which reduced electron scattering by surface defects and thereby enhanced the $\mu$ of ETLs. The electron transport of different ETLs from perovskite to FTO was characterized using time-resolved PL (TRPL) spectroscopy, as shown in Figure 3C. The average lifetimes ($\tau_{ave}$) of TRPL curves were obtained through biexponential fitting and are listed in Table S3. The strongest carrier-extraction capability was found in the PBBP-$SnO_2$ ETL/perovskite sample, with $\tau_{ave}$ of 202.02 ns, significantly lower than that of 475.61 ns for the $SnO_2$/perovskite counterpart.

The influence of different ETLs on the crystallinity and morphology of perovskite was characterized by the combination of X-ray diffraction (XRD) technique, PL spectroscopy, confocal laser scanning microscopy (CLSM), and XPS. As shown in Figure 3D, compared to the $SnO_2$ ETL, the crystallinity of perovskite on the PBBP-$SnO_2$ ETL has been improved, while that of the MBBM-$SnO_2$ ETL counterpart has been decreased. As shown in Figure S19, the PL peak of the perovskite induced by the PBBP-$SnO_2$ ETL (817 nm) has blue-shifted by 3 nm compared to the $SnO_2$ ETL (820 nm), indicating a decrease in defect density in the perovskite. However, the perovskite of the MBBM-$SnO_2$ sample has shown an opposite shift by 1 nm, indicating a reduced perovskite crystallinity, which is consistent with the XRD results (Figure 3D). This was mainly due to the weaker chelating capability of MBBM with $SnO_2$, which resulted in MBBM precipitation during ETL deposition and led to a non-uniform crystallization of perovskite (Figure S20). We further characterized the PL uniformity and grain-size distribution of perovskite on different ETLs by the CLSM method. As shown in Figure 3E, the perovskite on the PBBP-$SnO_2$ ETL exhibits a more uniform PL intensity compared to the other three counterparts. The AGS of the perovskite on the PBBP-$SnO_2$ ETL is 2.22 μm, obviously larger than that of $SnO_2$ (1.83 μm), MBBM-$SnO_2$ (1.32 μm), and PBP-$SnO_2$ (1.87 μm), as shown in Figure 3F. This mainly

originated from the high homogeneity, reduced defect density, and effective chelating with unsaturated $Pb^{2+}$ of the PBBP-$SnO_2$ ETL, represented as $Pb^0$/($Pb^0$+ $Pb^{2+}$), which promoted the uniform nucleation and growth of perovskite (Figures S21 and S22).[45]

Combined with the induction effect on perovskite growth, the PBBP-$SnO_2$ ETL can simultaneously achieve effective electron extraction from perovskite and electron transport to FTO, thereby achieving a balance in the interface carrier dynamics.

## Device performance

We fabricated PSCs with the architecture of anti-reflection layer/glass/FTO/ETL/perovskite/CsI/n-octylammonium iodide (OAI)/2,2′,7,7′-tetrakis(*N*,*N*-di-*p*-methoxyphenylamine)-9,9′-spirobifluorene (spiro-OMeTAD)/Au. The SEM image of the PSCs equipped with a PBBP-$SnO_2$ ETL is shown in Figure 4A. Among the three types of TCM-ETLs, the PSCs with PBBP-$SnO_2$ ETL shows the largest quasi-Fermi-level splitting (QFLS) of 1.171 eV, obviously superior to the results of PSCs with MBBM-$SnO_2$ (1.141 eV) and PBP-$SnO_2$ (1.145 eV), as shown in Figure 4B (for details see Note S8). Therefore, the PSC with PBBP-$SnO_2$ ETL was selected (denoted as TCM device) to compare it with the $SnO_2$-ETL counterpart (denoted as control device). The current density-voltage (*J-V*) curves of the champion devices with an aperture area of 0.09 $cm^2$ are shown in Figure 4C, and detailed parameters are listed in Table S4. The TCM device obtained a PCE of 25.32% under reverse scan with a $V_{OC}$ of 1.16 V, short-circuit current ($J_{SC}$) of 25.94 mA $cm^{-2}$, and FF of 84.13%. The control device also yielded a high PCE of 23.59% with a $V_{OC}$ of 1.13 V, $J_{SC}$ of 25.71 mA $cm^{-2}$, and FF of 81.21%. The $J_{SC}$ of the TCM device matches well with the integrated *J* of 25.34 mA $cm^{-2}$ that is calculated from the incident photon-to-current efficiency (IPCE) spectrum, with a mismatch of less than 3%, as shown in Figure 4D.

We further fabricated the devices with an aperture area of 1.00 $cm^2$. The *J-V* curves and corresponding detailed performance parameters are shown in Figure S23 and Table S4, respectively As shown in Figure 4E, the control device shows an obvious efficiency loss from 23.59% (0.09 $cm^2$) to 21.60% (1.00 $cm^2$), while that loss is minimized for the TCM device, mostly owing to the retention of the high FF of 83.25%. The 1-$cm^2$ TCM device exhibits a champion PCE of 24.57% under reverse scan. Notably, the relative efficiency loss (Note S9) for devices with aperture areas from 0.09 to 1.00 $cm^2$ is reduced from 8.44% (control device) to 2.96% (TCM device), indicating the high efficiency and scalability of TCM devices. Furthermore, the TCM device with aperture area of 10.89 $cm^2$ achieves a PCE of 21.81% (Figures S24 and S25; Table S5). The efficiency degradation rate of TCM devices with aperture areas from 0.09 to 10.89 $cm^2$ is only $-0.325$ $cm^{-2}$, which is well below that of representative certified perovskite photovoltaic devices ($-1.498$ $cm^{-2}$) (Figure S26).

The operational stability of TCM devices is also substantially improved compared with control counterparts (Figure 4F; for test details, see methods). The detailed parameters of the control and TCM devices for stability testing are summarized in Table S6. The PCE of the encapsulated control device dropped by 10% and 57% after 600 and 1,632 h, respectively, following the ISOS-L-3 protocol. On the contrary, the TCM device maintained 90% of the initial PCEs after 1,632 h, which is mainly due to the stable interface charge dynamics by the self-assembled conformal PBBP-$SnO_2$ ETL with reduced defect-assisted charge accumulation and recombination.[46,47] The detailed parameters of the control and TCM device after 1,632 h of stability testing are summarized in Table S7. This hypothesis has been validated through the QFLS decay of control devices by 0.302 eV as the operational stability testing is extended, whereas the QFLS of the TCM device is merely reduced by 0.096 eV before and after aging (Figure S27).

As shown in Figure S28, after undergoing operational stability tests for 100, 400, and 600 h, the perovskite films from the TCM device degraded slowly. For the ETL samples, the TCM-$SnO_2$ sample under conditions of 65°C and ca. 50% relative humidity for 100, 400, 600, and 800 h did not exhibit visible alterations, while the $SnO_2$ sample began to show noticeable morphological damage after 600 h of aging (Figure S29). Subsequently, the perovskite film from the control device showed initial degradation at 600 h, and significant damage was already evident at 800 h. The results of UV-visible (UV-vis) absorption spectra are consistent with the SEM images of perovskite (Figure S30).

Furthermore, time-of-flight secondary-ion mass spectrometry (ToF-SIMS) was used to characterize the ion distribution of perovskite in the control and TCM devices. As shown in Figure S31, $I^-$ ions from the perovskite layer gradually show small-scale diffusion after aging for 100, 400, 600m and 800 h in TCM devices, while significant diffusion of $I^-$ occurs after 800 h in the control device, consistent with the SEM results. In the XPS spectra of the O 1s core level of $SnO_2$, the proportion of $O_{defect}$ after aging for 100, 400, 600, and 800 h are 55.34%, 56.41%, 63.28%, and 78.32%, respectively (Figure S32A). Conversely, the proportion of $O_{defect}$ in TCM-$SnO_2$ does not show significant changes from 0 to 800 h (Figures S9A and S32B).

Therefore, the efficiency decay of the control device within the 600 h is mainly due to the degradation of the perovskite itself. After 600 h, significant disruption of the $SnO_2$ in the control device leads to extensive fractures of the bonds at the $SnO_2$/perovskite interface, which further triggers the rapid degradation of perovskite and results in a fast decay of the control device. In the TCM device, the passivation of TCMs for the surface defects of $SnO_2$ and the formation of a stable $SnO_2$/perovskite interface reduced defect-assisted charge accumulation and inhibited the rapid degradation of perovskite.

In summary, we propose a targeted chelating strategy to create a self-assembled conformal $SnO_2$ ETL through solution processing on a textured TCO surface for large-area PSCs. The two terminal groups of PBBP can target chelation with $V_O$ of $SnO_2$ nanoparticles to form a quasi-monomer dispersion and establish robust bonds with $F_O$ of FTO during ETL deposition. Benefiting from the balanced interface charge dynamics, the corresponding PSCs achieved champion PCEs of 25.32% and 24.57% under reverse scan with aperture areas of 0.09 and 1.00 $cm^2$, respectively, passing the ISOS-L-3 protocol. We anticipate that this work will open new avenues for designing conformal charge transport layers to enhance the efficiency, scalability, and stability of PSCs.

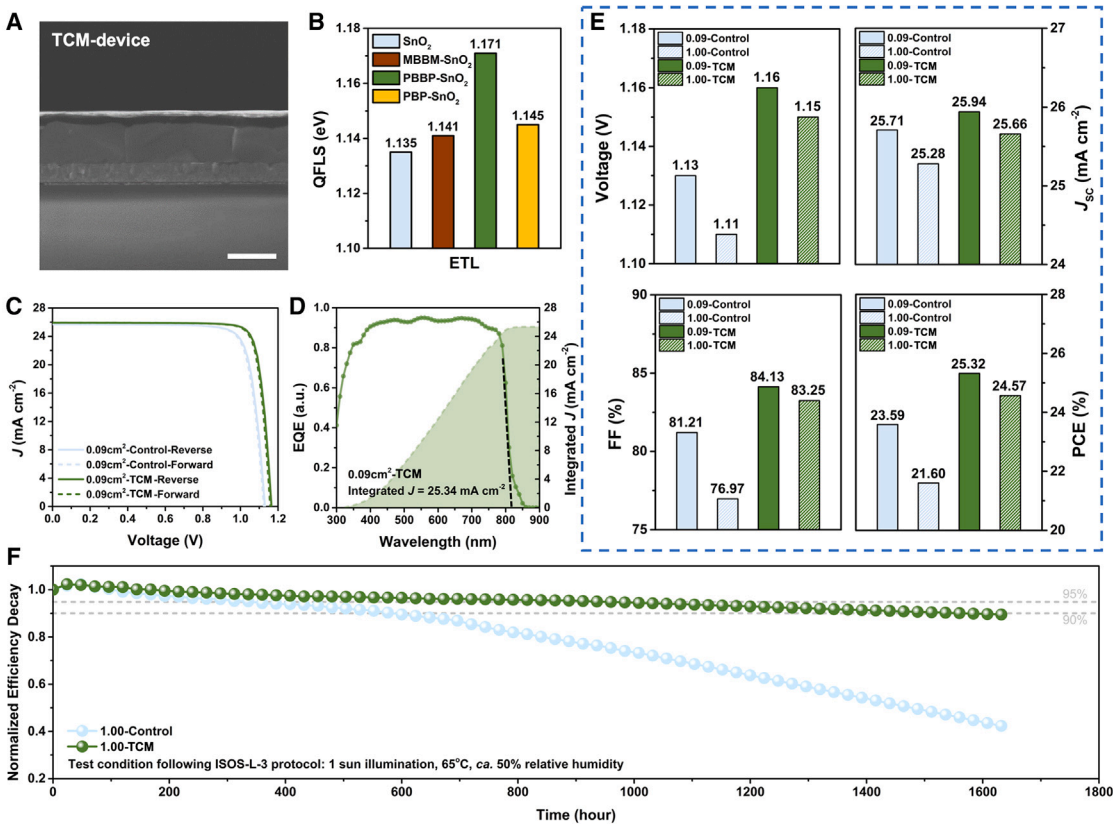


**Figure 4. Efficiency, scalability, and stability of TCM devices**

(A) Cross-sectional images of SEM of TCM devices. Scale bar, 1 μm.

(B) QFLS of PSCs equipped with $SnO_2$ ETL modified with or without TCMs.

(C and D) (C) *J-V* curves of champion control and TCM devices with an aperture area of 0.09 $cm^2$. (D) Corresponding IPCE and integrated *J* of champion TCM device with an aperture area of 0.09 $cm^2$. The intersection of the dashed line with the x axis indicates the position of the absorption edge, and the slow increase starting from 850 nm belongs to the band-edge absorption due to the disturbances originating from the presence of impurities in the perovskite material, which does not affect the position of absorption edge.

(E) Relationship between performance parameters and aperture area of champion control and TCM device.

(F) Operational stability of the control and TCM devices with an aperture area of 1 $cm^2$ following the ISOS-L-3 protocol (maximum power point, continuous 1 sun illumination, 65°C, and ca. 50% relative humidity). All the cells were encapsulated, and the initial PCEs of control and TCM devices are 20.45% and 22.51%, respectively, mainly due to the replacement of hole transport layers.

## METHODS

### Materials

All chemicals were purchased from companies without further purification. ETL: dispersing $SnO_2$, 15% in $H_2O$ colloidal dispersion (Alfa Aesar), deionized water (Sigma Aldrich), MBBM (97%, Aladdin), PBBP (>97%, Aladdin), PBP (>98%, Tokyo Chemical Industry), and KOH (>86%, Tokyo Chemical Industry). Perovskite precursor: $CH(NH_2)_2I$ (FAI, 98%), $CH_3NH_3I$ (MAI, 98%), $CH_3NH_3Cl$ (MACl, 98%), and $PbI_2$ (99.99%) from Tokyo Chemical Industry; dimethylformamide (DMF, 99.8%), dimethyl sulfoxide (DMSO, 99.9%), and isopropanol (IPA, 99.5%) from Sigma-Aldrich. Passivation layer: CsI (>99%), OAI (>98%) from Tokyo Chemical Industry. HTL: spiro-OMeTAD (99.8%) from Ningbo Borun New Material Technology; 4-*tert*-butylpyridine (*t*BP, 96%), Li-TFSI (99.95%), acetonitrile (ACN, 99.8%), and chlorobenzene (CB, 99.8%) from Sigma-Aldrich; polytriarylamine (PTAA) from Sigma-Aldrich); 4-isopropyl-4′-methyldiphenyliodonium tetrakis(pentafluorophenyl) borate (TPFB, >98%) from Tokyo Chemical Industry. Buffer layer: $MoO_3$ (99.998%) from Alfa Aesar. Electrode: Au (99.999%) from Beijing Dream Material Technology.

### Components of ETLs

(1) $SnO_2$ dispersion: diluting dispersing $SnO_2$ by deionized water with v/v of 1:8.5; MBBM-$SnO_2$ dispersion: 0.0353 g of MBBM was dissolved in 8.5 mL of deionized water with KOH to modify the pH value (denoted as MBBM-KOH, M(KOH)/M(MBBM) = 3.5), after which 1 mL of dispersing $SnO_2$ was diluted in 8.5 mL of MBBM-KOH to form MBBM-$SnO_2$ dispersion. (2) PBBP-$SnO_2$ dispersion: 0.0458 g of PBBP was dissolved in 8.5 mL of deionized water with KOH to modify the pH value (denoted as PBBP-KOH, M(KOH)/M(PBBP) = 5.0), after which 1 mL of dispersing $SnO_2$ was diluted in 8.5 mL of PBBP-KOH to form PBBP-$SnO_2$ dispersion. (3) 0.0348 g of PBP was dissolved in 8.5 mL of deionized water with KOH to modify the pH value

(denoted as PBP-KOH, M(KOH)/M(PBP) = 5.0), after which 1 mL of dispersing $SnO_2$ was diluted in 8.5 mL of PBP-KOH to form PBP-$SnO_2$ dispersion.

### Fabrication of anti-reflection layers

A precursor solution composed of methyl isobutyl ketone and silicon dioxide nanoparticles was purchased from Shanghai Juanrou Newtech and diluted by IPA (1:1 v/v). The diluted solution was spin coated atop the glass side of FTO substrates at 3,000 rpm for 30 s, followed by a thermal annealing process at 120°C for 2 h to remove the solvent and obtain the anti-reflection layer.

### Fabrication of PSCs

The FTO substrates were etched with zinc powder and 6 M aqueous hydrochloric acid for 15 s to obtain patterned substrates. The patterned substrates were then sonicated with detergent, deionized water, ethanol, acetone, and IPA, respectively for 15 min. The sheet resistance and average transmittance in the visible-light wavelength range of FTO substrate used for preparing 0.09-$cm^2$ devices and 1-$cm^2$ devices are 10 Ω/□ and 89%, respectively. The FTO substrate used for preparing 10-$cm^2$ devices has a sheet resistance and average transmittance in the visible-light wavelength range of 6 Ω/□ and 88%, respectively. After drying, the FTO substrates were cleaned with UV ozone for 20 min. Different $SnO_2$ dispersions were then spin coated on the substrate at 3,000 rpm for 30 s to form $SnO_2$ ETLs, followed by annealing in ambient air at 150°C for 30 min. After being cleaned with UV ozone for 20 min, the substrates were transferred to an $N_2$-filled glovebox. Next, 1.5 M $PbI_2$ in DMF/DMSO (9:1 v/v) was spin coated on the $SnO_2$ ETL at 1,500 rpm for 40 s and annealed at 70°C for 1 min. A solution of FAI/MAI/MACl (90:13:9 mg) dissolved in 1 mL of IPA was then dynamically spin coated on $PbI_2$ films at 1,800 rpm for 30 s, followed by annealing for 15 min at 150°C under ambient atmosphere (30%–34% relative humidity). After being transferred to the $N_2$-filled glovebox and cooled down, a passivation layer of CsI with 5 nm was deposited by thermal evaporation, and a passivation layer of OAI solution (5 mg in 1 mL IPA) was spin coated on perovskite at a spin rate of 5,000 rpm for 30 s before the HTL deposition. For the spiro-OMeTAD ETL with Li-TFSI, 72.3 mg of spiro-OMeTAD, 17.5 μL of Li-TFSI (520 mg Li-TFSI in 1 mL ACN), and 28.8 μL of *t*BP were dissolved in 1 mL of CB and spin coated atop perovskite film at a spin rate of 3,000 rpm for 30 s. For the PTAA ETL for stability tests, 30 mg of PTAA HTLs doped with 3 mg of TPFB in 1 mL of toluene was spin coated atop perovskite film at a spin rate of 2,000 rpm for 30 s. The 120-nm Au electrodes were then thermally evaporated as anodes using a shadow mask with a substrate cooling system. The 0.09-$cm^2$ and 1.00-$cm^2$ (0.50 cm × 2.00 cm) masks were used to define the active areas during measurements.

### Characterization

The ATR-IR images were acquired using a Nicolet 6700 instrument (Thermo Fisher, USA). The spectra were referenced to the spectrum of the $BaF_2$ substrates in their bare form, with the spectral range and resolution set at 400–4,000 $cm^{-1}$ and 4 $cm^{-1}$, respectively. The XPS and UPS results were obtained using an AXIS UltraDLD instrument with an Al Kα X-ray source (AXIS, China). The signals were calibrated using the peaks of the C 1s core level due to its relatively consistent binding energy. DLS spectra were measured by Omni (Brookhaven, USA) with the testing range for particle size from 0.3 nm to 10 μm. The TEM images were captured using a Talos F200X G2 system (Talos, USA) equipped with EDS capabilities. The cross-sectional samples were prepared using the focused ion beam (FIB) technique with a GAIA3 instrument (GAI, Czech Republic). To minimize environmental effects and potential damage from the high-energy FIB, a 2-μm carbon (C) layer was deposited over the Pt layers. To mitigate heat-induced sample alterations, a lower FIB voltage of 5 kV was utilized. The AGS of $SnO_2$ grains is derived from grain statistics by the open-access ImageJ application. AFM was carried out on an MFP-3D (Oxford Instruments, USA) to measure the sample roughness. The Fastscan Bio AFM system (Bruker, USA) equipped with a Multi75E-G tip was used to acquire the conductive AFM images. The pH values of TCM solution and corresponding $SnO_2$ dispersion was measured by a pH meter (S220, China). The Agilent Cary 670 FTIR spectrometer, in conjunction with a Cary 620 microscope featuring a focal plane array detector (iN10 MX, Thermo Scientific, USA), was employed for acquiring FTIR microscopy images. The instrument has a spatial resolution of 5.5 μm per pixel with a total of 64 × 64 pixels. IR mapping spectra were gathered in ambient air utilizing non-polarized light-transmission mode. For all spectra, reference was made to the spectrum of the pristine $BaF_2$ substrate, and the spectral resolution was maintained at 4 $cm^{-1}$. The transmittance spectra were analyzed through UV-vis absorption spectroscopy using a Lamda 950 instrument (Lamda, China). The current-voltage curves were measured with a Keithley 2400 digital source meter under dark conditions. A JEOL JSM-7800F Prime field-emission scanning electron microscope (JEOL, Japan) was utilized to examine the morphology of the samples. The TRPL and PL spectra were measured on an FLS1000 system (Edinburgh Instruments, UK), and fitted by the bi-exponential formulas (Equations S12 and S13).[48] The XRD patterns were obtained using a multifunctional X-ray diffractometer (D8 Advance, Da Vinci, Germany) with a scanning range from 3° to 70° at a scanning rate of 0.3° per second. CLSM images of perovskite atop different $SnO_2$ ETLs were tested by TCS SP8 STED 3X (Leica, Germany). The AGS of perovskite grains is derived from grain statistics by the open-access ImageJ application. The QFLS results were measured by a photoluminescence quantum yield (PLQY) system (Quantaurus-QY Pllus, China), and details of the analysis can be found in Note S8. The SCLC method was measured by a multifunctional electrochemical analysis instrument (Zahner, Germany). The *J-V* characteristics of PSCs were obtained under simulated solar illumination of 100 mW $cm^{-2}$, air mass 1.5 global spectrum using a WXS-155S-10 solar simulator (Wacom Denso) and recorded with a digital source meter. The solar simulator was calibrated using a standard silicon reference cell certified by the Calibration, Standards and Measurement Team at the Research Center for Photovoltaics in AIST, Japan, ensuring a spectral mismatch of less than 3%. The *J-V* measurements were conducted during forward scan (−0.2 to 1.2 V) or reverse scan (1.2 to −0.2 V)

sweeps. The IPCE spectrum was determined using monochromatic light with an intensity of $1 \times 10^{16}$ photons $cm^{-2}$. ToF-SIMS results were based on an IONTOF SIMS 5-100 (IONTOF, Germany) with a stable $Cs^+$ ion beam as the ion beam to peel off the sample with a detected area of $100 \times 100$ $\mu m^2$.

### Operational stability test of PSCs based on the ISOS-L-3 protocol

To assess the operational stability shown in Figure 4F, PTAA was used instead of spiro-OMeTAD to eliminate concerns about the thermal stability of HTLs. In this case, PTAA was doped with TPFB instead of Li-TFSI and *t*BP. The 5-nm $MoO_3$ buffer layer was inserted between PTAA and Au electrode to reduce Au migration from electrodes. The PSCs were encapsulated in the nitrogen-filled glovebox with cavity glass and UV-curable glue based on our previous work.[49] The operational stability of the encapsulated PSCs was evaluated using a solar cell light resistance testing system following the ISOS-L-3 protocol, with measurements taken at the maximum power point under standard 1-sun illumination (100 mW $cm^{-2}$) with 65°C and ca. 50% relative humidity. The PCE of the PSCs mentioned above was monitored every 24 h using the reverse *J-V* scan.

## RESOURCE AVAILABILITY

### Lead contact

Further information and requests for resources should be directed to and will be fulfilled by the lead contact, Wenzhong Shen (wzshen@sjtu.edu.cn).

### Materials availability

This study did not generate new, unique materials.

### Data and code availability

- All data reported in this paper will be shared by the lead contact upon request.
- This paper does not report original code.
- Any additional information required to reanalyze the data reported in this paper is available from the lead contact upon request.

## ACKNOWLEDGMENTS

This work was supported by the Natural Science Foundation of China (11834011) and Shanghai New Energy Technology Research and Development Project 24DZ3000900. The authors thank the Instrumental Analysis Center of Shanghai Jiao Tong University for assistance with the characterizations.

## AUTHOR CONTRIBUTIONS

Conceived the work: H.S. and W.S.; fabricated solar cells: H.S.; conducted UV-vis, ATR-IR, FTIR, DLS, conductive AFM, TEM, AFM, Kelvin probe force microscopy, XPS, UPS, QFLS, SEM, XRD, and CLSM: H.S. and X.L.; *J-V* and IPCE measurements: H.S.; assisted with measurement of UV-vis: L.H.; assisted with analysis of CLSM: C.G. and D.Z.; assisted with analysis of UPS: D.D. and H.L.; wrote the first draft of the manuscript: H.S.; revised the manuscript: H.S., X.L., and W.S.; analyzed the data and reviewed the manuscript: all authors.

## DECLARATION OF INTERESTS

The authors declare no conflict of interests.

## SUPPLEMENTAL INFORMATION

Supplemental information can be found online at https://doi.org/10.1016/j.xcrp.2025.102506.

Received: October 28, 2024
Revised: December 21, 2024
Accepted: February 25, 2025
Published: March 25, 2025

## REFERENCES

1. Kojima, A., Teshima, K., Shirai, Y., and Miyasaka, T. (2009). Organometal halide perovskites as visible-light sensitizers for photovoltaic cells. J. Am. Chem. Soc. *131*, 6050–6051. https://doi.org/10.1021/ja809598r.
2. Kim, H.-S., Lee, C.-R., Im, J.-H., Lee, K.-B., Moehl, T., Marchioro, A., Moon, S.-J., Humphry-Baker, R., Yum, J.-H., Moser, J.E., et al. (2012). Lead iodide perovskite sensitized all-solid-state submicron thin film mesoscopic solar cell with efficiency exceeding 9%. Sci. Rep. *2*, 591. https://doi.org/10.1038/srep00591.
3. Yoo, J.J., Seo, G., Chua, M.R., Park, T.G., Lu, Y., Rotermund, F., Kim, Y.-K., Moon, C.S., Jeon, N.J., Correa-Baena, J.-P., et al. (2021). Efficient perovskite solar cells via improved carrier management. Nature *590*, 587–593. https://doi.org/10.1038/s41586-021-03285-w.
4. Chen, H., Liu, C., Xu, J., Maxwell, A., Zhou, W., Yang, Y., Zhou, Q., Bati, A.S.R., Wan, H., Wang, Z., et al. (2024). Improved charge extraction in inverted perovskite solar cells with dual-site-binding ligands. Science *384*, 189–193. https://doi.org/10.1126/science.adm9474.
5. Jiang, Q., Zhang, L., Wang, H., Yang, X., Meng, J., Liu, H., Yin, Z., Wu, J., Zhang, X., and You, J. (2016). Enhanced electron extraction using $SnO_2$ for high-efficiency planar-structure $HC(NH_2)(2)PbI_3$-based perovskite solar cells. Nat. Energy *2*, 16177. https://doi.org/10.1038/nenergy.2016.177.
6. Jiang, Q., Zhang, X., and You, J. (2018). $SnO_2$: A wonderful electron transport layer for perovskite solar cells. Small *14*, 1801154. https://doi.org/10.1002/smll.201801154.
7. Min, H., Lee, D.Y., Kim, J., Kim, G., Lee, K.S., Kim, J., Paik, M.J., Kim, Y.K., Kim, K.S., Kim, M.G., et al. (2021). Perovskite solar cells with atomically coherent interlayers on $SnO_2$ electrodes. Nature *598*, 444–450. https://doi.org/10.1038/s41586-021-03964-8.
8. Rong, Y., Hu, Y., Mei, A., Tan, H., Saidaminov, M.I., Seok, S.I., McGehee, M.D., Sargent, E.H., and Han, H. (2018). Challenges for commercializing perovskite solar cells. Science *361*, eaat8235. https://doi.org/10.1126/science.aat8235.
9. Li, N., Niu, X., Li, L., Wang, H., Huang, Z., Zhang, Y., Chen, Y., Zhang, X., Zhu, C., Zai, H., et al. (2021). Liquid medium annealing for fabricating durable perovskite solar cells with improved reproducibility. Science *373*, 561–567. https://doi.org/10.1126/science.abh3884.
10. Chen, H., Ye, F., Tang, W., He, J., Yin, M., Wang, Y., Xie, F., Bi, E., Yang, X., Grätzel, M., and Han, L. (2017). A solvent- and vacuum-free route to large-area perovskite films for efficient solar modules. Nature *550*, 92–95. https://doi.org/10.1038/nature23877.
11. Bu, T., Ono, L.K., Li, J., Su, J., Tong, G., Zhang, W., Liu, Y., Zhang, J., Chang, J., Kazaoui, S., et al. (2022). Modulating crystal growth of formamidinium-caesium perovskites for over 200 cm photovoltaic sub-modules. Nat. Energy *7*, 528–536. https://doi.org/10.1038/s41560-022-01039-0.
12. Su, H., Lin, X., Wang, Y., Liu, X., Qin, Z., Shi, Q., Han, Q., Zhang, Y., and Han, L. (2022). Stable perovskite solar cells with 23.12% efficiency and area over 1 cm(2) by an all-in-one strategy. Sci. China Chem. *65*, 1321–1329. https://doi.org/10.1007/s11426-022-1244-y.
13. Jung, E.H., Jeon, N.J., Park, E.Y., Moon, C.S., Shin, T.J., Yang, T.Y., Noh, J.H., and Seo, J. (2019). Efficient, stable and scalable perovskite solar cells using poly(3-hexylthiophene). Nature *567*, 511–515. https://doi.org/10.1038/s41586-019-1036-3.

14. Jeon, N.J., Na, H., Jung, E.H., Yang, T.Y., Lee, Y.G., Kim, G., Shin, H.W., Il Seok, S., Lee, J., and Seo, J. (2018). A fluorene-terminated hole-transporting material for highly efficient and stable perovskite solar cells. Nat. Energy *3*, 682–689. https://doi.org/10.1038/s41560-018-0200-6.

15. Bu, T., Li, J., Zheng, F., Chen, W., Wen, X., Ku, Z., Peng, Y., Zhong, J., Cheng, Y.-B., and Huang, F. (2018). Universal passivation strategy to slot-die printed $SnO_2$ for hysteresis-free efficient flexible perovskite solar module. Nat. Commun. *9*, 4609. https://doi.org/10.1038/s41467-018-07099-9.

16. Siegrist, S., Nandi, P., Kothandaraman, R.K., Abdessalem, A., Tiwari, A.N., and Fu, F. (2023). Understanding coating thickness and uniformity of blade-coated SnO electron transport layer for scalable perovskite solar cells. Sol. RRL *7*, 2300273. https://doi.org/10.1002/solr.202300273.

17. Smith, J.A., Game, O.S., Bishop, J.E., Spooner, E.L.K., Kilbride, R.C., Greenland, C., Jayaprakash, R., Alanazi, T.I., Cassella, E.J., Tejada, A., et al. (2020). Rapid scalable processing of tin oxide transport layers for perovskite solar cells. ACS Appl. Energy Mater. *3*, 5552–5562. https://doi.org/10.1021/acsaem.0c00525.

18. Zhang, J., Bai, C., Dong, Y., Shen, W., Zhang, Q., Huang, F., Cheng, Y.B., and Zhong, J. (2021). Batch chemical bath deposition of large-area $SnO_2$ film with mercaptosuccinic acid decoration for homogenized and efficient perovskite solar cells. Chem. Eng. J. *425*, 131444. https://doi.org/10.1016/j.cej.2021.131444.

19. Erdenebileg, E., Wang, H., Li, J., Singh, N., Dewi, H.A., Tiwari, N., Mathews, N., Mhaisalkar, S., and Bruno, A. (2022). Low-temperature atomic layer deposited electron transport layers for Co-evaporated perovskite solar cells. Sol. RRL *6*, 2100842. https://doi.org/10.1002/solr.202100842.

20. Bai, Y., Huang, Z., Zhang, X., Lu, J., Niu, X., He, Z., Zhu, C., Xiao, M., Song, Q., Wei, X., et al. (2022). Initializing film homogeneity to retard phase segregation for stable perovskite solar cells. Science *378*, 747–754. https://doi.org/10.1126/science.abn3148.

21. Bu, T., Liu, X., Zhou, Y., Yi, J., Huang, X., Luo, L., Xiao, J., Ku, Z., Peng, Y., Huang, F., et al. (2017). A novel quadruple-cation absorber for universal hysteresis elimination for high efficiency and stable perovskite solar cells. Energy Environ. Sci. *10*, 2509–2515. https://doi.org/10.1039/c7ee02634j.

22. Jiang, Q., Zhao, Y., Zhang, X., Yang, X., Chen, Y., Chu, Z., Ye, Q., Li, X., Yin, Z., and You, J. (2019). Surface passivation of perovskite film for efficient solar cells. Nat. Photonics *13*, 460–466. https://doi.org/10.1038/s41566-019-0398-2.

23. Anaraki, E.H., Kermanpur, A., Steier, L., Domanski, K., Matsui, T., Tress, W., Saliba, M., Abate, A., Grätzel, M., Hagfeldt, A., and Correa-Baena, J.P. (2016). Highly efficient and stable planar perovskite solar cells by solution-processed tin oxide. Energy Environ. Sci. *9*, 3128–3134. https://doi.org/10.1039/c6ee02390h.

24. Tavakoli, M.M., Giordano, F., Zakeeruddin, S.M., and Grätzel, M. (2018). Mesoscopic oxide double layer as electron specific contact for highly efficient and UV stable perovskite photovoltaics. Nano Lett. *18*, 2428–2434. https://doi.org/10.1021/acs.nanolett.7b05469.

25. Yang, M., Qin, Z., Chen, M., Lin, X., Luan, X., Yang, Z., Han, L., and Wang, Y. (2024). Building scalable buried interface for high-performance perovskite photovoltaic devices. Adv. Funct. Mater. *34*, 2402053. https://doi.org/10.1002/adfm.202402053.

26. Xiao, K., Lin, R., Han, Q., Hou, Y., Qin, Z., Nguyen, H.T., Wen, J., Wei, M., Yeddu, V., Saidaminov, M.I., et al. (2020). All-perovskite tandem solar cells with 24.2% certified efficiency and area over 1 cm(2) using surface-anchoring zwitterionic antioxidant. Nat. Energy *5*, 870–880. https://doi.org/10.1038/s41560-020-00705-5.

27. Kim, M., Jeong, J., Lu, H., Lee, T.K., Eickemeyer, F.T., Liu, Y., Choi, I.W., Choi, S.J., Jo, Y., Kim, H.-B., et al. (2022). Conformal quantum dot $SnO_2$ layers as electron transporters for efficient perovskite solar cells. Science *375*, 302–306. https://doi.org/10.1126/science.abh1885.

28. Sun, X., Wang, Q., Wei, J., and Li, H. (2021). Polymer network modified mesoporous $SnO_2$ for enhanced fill factor in perovskite solar cells. ACS Appl. Energy Mater. *4*, 7481–7486. https://doi.org/10.1021/acsaem.1c01090.

29. Dong, Q., Wang, M., Zhang, Q., Chen, F., Zhang, S., Bian, J., Ma, T., Wang, L., and Shi, Y. (2017). Discontinuous $SnO_2$ derived blended-interfacial-layer in mesoscopic perovskite solar cells: Minimizing electron transfer resistance and improving stability. Nano Energ *38*, 358–367. https://doi.org/10.1016/j.nanoen.2017.05.058.

30. Wang, M., Zhao, Y., Jiang, X., Yin, Y., Yavuz, I., Zhu, P., Zhang, A., Han, G.S., Jung, H.S., Zhou, Y., et al. (2022). Rational selection of the polymeric structure for interface engineering of perovskite solar cells. Joule *6*, 1032–1048. https://doi.org/10.1016/j.joule.2022.04.002.

31. Wu, T., Wang, Y., Li, X., Wu, Y., Meng, X., Cui, D., Yang, X., and Han, L. (2019). Efficient defect passivation for perovskite solar cells by controlling the electron density distribution of donor-π-acceptor molecules. Adv. Energy Mater. *9*, 1803766. https://doi.org/10.1002/aenm.201803766.

32. Zhang, S., Wu, R., Mu, C., Wang, Y., Han, L., Wu, Y., and Zhu, W.H. (2022). Conjugated self-assembled monolayer as stable hole-selective contact for inverted perovskite solar cells. ACS Mater. Lett. *4*, 1976–1983. https://doi.org/10.1021/acsmaterialslett.2c00799.

33. Li, N., Niu, X., Pei, F., Liu, H., Cao, Y., Liu, Y., Xie, H., Gao, Y., Chen, Q., Mo, F., and Zhou, H. (2020). Energy-level modulation in diboron-modified $SnO_2$ for high-efficiency perovskite solar cells. Sol. RRL *4*, 1900217. https://doi.org/10.1002/solr.201900217.

34. Wang, X., Wang, X., Di, Q., Zhao, H., Liang, B., and Yang, J. (2017). Mutual effects of fluorine dopant and oxygen vacancies on structural and luminescence characteristics of F doped $SnO_2$ nanoparticles. Materials *10*, 1398. https://doi.org/10.3390/ma10121398.

35. Das, S., and Jayaraman, V. (2015). $SnO_2$: A comprehensive review on structures and gas sensors. Prog. Mater. Sci. *67*, 161. https://doi.org/10.1016/j.pmatsci.2014.10.001.

36. Shah, K.H., Mustafa, S., Waseem, M., Hamayun, M., Shah, F., Rehman, W., and Khan, A.R. (2017). Competitive exchange of Cr (III) sorption on macroporous Amberlyst.15 (H). Mater. Res. Express *4*, 015502. https://doi.org/10.1088/2053-1591/aa5469.

37. Zhang, B., Huang, H.J., and Ramaswamy, S. (2012). A kinetics study on hydrothermal liquefaction of high-diversity grassland perennials. Energy Sources, Part A Recovery, Util. Environ. Eff. *34*, 1676–1687. https://doi.org/10.1080/15567036.2010.483453.

38. Andras, B. (2009). A polarizable, four-point-charge model of water with size variation. J. Mol. Liq. *148*, 88–93. https://doi.org/10.1016/j.molliq.2009.06.013.

39. Chen, W., Wu, Y., Liu, J., Qin, C., Yang, X., Islam, A., Cheng, Y.B., and Han, L. (2015). Hybrid interfacial layer leads to solid performance improvement of inverted perovskite solar cells. Energy Environ. Sci. *8*, 629–640. https://doi.org/10.1039/c4ee02833c.

40. Zhou, H., Chen, Q., Li, G., Luo, S., Song, T.B., Duan, H.S., Hong, Z., You, J., Liu, Y., and Yang, Y. (2014). Interface engineering of highly efficient perovskite solar cells. Science *345*, 542–546. https://doi.org/10.1126/science.1254050.

41. Lin, X., Wang, Y., Su, H., Qin, Z., Zhang, Z., Chen, M., Yang, M., Zhao, Y., Liu, X., Shen, X., and Han, L. (2022). An in-situ formed tunneling layer enriches the options of anode for efficient and stable regular perovskite solar cells. Nano-Micro Lett. *15*, 10. https://doi.org/10.1007/s40820-022-00975-6.

42. Zhou, Y., Fuentes-Hernandez, C., Shim, J., Meyer, J., Giordano, A.J., Li, H., Winget, P., Papadopoulos, T., Cheun, H., Kim, J., et al. (2012). A Universal method to produce low-work function electrodes for organic electronics. Science *336*, 327–332. https://doi.org/10.1126/science.1218829.

43. Kim, G., Min, H., Lee, K.S., Lee, D.Y., Yoon, S.M., and Seok, S.I. (2020). Impact of strain relaxation on performance of alpha-formamidinium lead iodide perovskite solar cells. Science *370*, 108–112. https://doi.org/10.1126/science.abc4417.

44. Min, H., Kim, M., Lee, S.U., Kim, H., Kim, G., Choi, K., Lee, J.H., and Seok, S.I. (2019). Efficient, stable solar cells by using inherent bandgap of alpha-phase formamidinium lead iodide. Science *366*, 749–753. https://doi.org/10.1126/science.aay7044.

45. Wang, L., Zhou, H., Hu, J., Huang, B., Sun, M., Dong, B., Zheng, G., Huang, Y., Chen, Y., Li, L., et al. (2019). A $Eu^{3+}$-$Eu^{2+}$ ion redox shuttle imparts operational durability to Pb-I perovskite solar cells. Science *363*, 265–270. https://doi.org/10.1126/science.aau5701.

46. Li, Z., Li, B., Wu, X., Sheppard, S.A., Zhang, S., Gao, D., Long, N.J., and Zhu, Z. (2022). Organometallic-functionalized interfaces for highly efficient inverted perovskite solar cells. Science *376*, 416–420. https://doi.org/10.1126/science.abm8566.

47. Azmi, R., Ugur, E., Seitkhan, A., Aljamaan, F., Subbiah, A.S., Liu, J., Harrison, G.T., Nugraha, M.I., Eswaran, M.K., Babics, M., et al. (2022). Damp heat-stable perovskite solar cells with tailored-dimensionality 2D/3D heterojunctions. Science *376*, 73–77. https://doi.org/10.1126/science.abm5784.

48. Lin, X., Su, H., He, S., Song, Y., Wang, Y., Qin, Z., Wu, Y., Yang, X., Han, Q., Fang, J., et al. (2022). In situ growth of graphene on both sides of a Cu–Ni alloy electrode for perovskite solar cells with improved stability. Nat. Energy *7*, 520–527. https://doi.org/10.1038/s41560-022-01038-1.

49. Chen, W., Wu, Y., Yue, Y., Liu, J., Zhang, W., Yang, X., Chen, H., Bi, E., Ashraful, I., Grätzel, M., and Han, L. (2015). Efficient and stable large-area perovskite solar cells with inorganic charge extraction layers. Science *350*, 944–948. https://doi.org/10.1126/science.aad1015.